Cerebral Cortex, November 2020;30: 5899–5914

doi: 10.1093/cercor/bhaa165
Advance Access Publication Date: 24 June 2020
Original Article

ORIGINAL ARTICLE

Propagation of BOLD Activity Reveals Task-dependent Directed Interactions Across Human Visual Cortex

Nicolás Gravel[1,2], Remco J. Renken[2,3], Ben M. Harvey[4], Gustavo Deco[5,6,7,8], Frans W. Cornelissen[2,†] and Matthieu Gilson[5,†]

[1]Neural Dynamics of Visual Cognition Group, Department of Education and Psychology, Freie University Berlin, 14195 Berlin, Germany, [2]Laboratory of Experimental Ophthalmology, University Medical Center Groningen, University of Groningen, 9713 GZ Groningen, The Netherlands, [3]Cognitive Neuroscience Center, University Medical Center Groningen, University of Groningen, 9713 GZ Groningen, The Netherlands, [4]Experimental Psychology, Helmholtz Institute, Utrecht University, 3584 CS Utrecht, The Netherlands, [5]Center for Brain and Cognition, Computational Neuroscience Group, Department of Information and Communication Technologies, Universitat Pompeu Fabra, 08018 Barcelona, Spain, [6]Institució Catalana de la Recerca i Estudis Avançats (ICREA), 08010 Barcelona, Spain, [7]Department of Neuropsychology, Max Planck Institute for Human Cognitive and Brain Sciences, 04103 Leipzig, Germany and [8]School of Psychological Sciences, Monash University, VIC 3800 Melbourne, Australia

Address correspondence to Nicolás Gravel, Neural Dynamics of Visual Cognition Group, Department of Education and Psychology, Freie Universität Berlin, D-14195 Berlin, German. Email: nicolas.gravel@fu-berlin.de.
[†]Frans W. Cornelissen and Matthieu Gilson shared last authorship to this work.

Abstract

It has recently been shown that large-scale propagation of blood-oxygen-level-dependent (BOLD) activity is constrained by anatomical connections and reflects transitions between behavioral states. It remains to be seen, however, if the propagation of BOLD activity can also relate to the brain's anatomical structure at a more local scale. Here, we hypothesized that BOLD propagation reflects structured neuronal activity across early visual field maps. To explore this hypothesis, we characterize the propagation of BOLD activity across V1, V2, and V3 using a modeling approach that aims to disentangle the contributions of local activity and directed interactions in shaping BOLD propagation. It does so by estimating the effective connectivity (EC) and the excitability of a noise-diffusion network to reproduce the spatiotemporal covariance structure of the data. We apply our approach to 7T fMRI recordings acquired during resting state (RS) and visual field mapping (VFM). Our results reveal different EC interactions and changes in cortical excitability in RS and VFM, and point to a reconfiguration of feedforward and feedback interactions across the visual system. We conclude that the propagation of BOLD activity has functional relevance, as it reveals directed interactions and changes in cortical excitability in a task-dependent manner.

Key words: BOLD activity propagation, functional neuroanatomy, network connectivity modeling, resting state, visual cortical maps

Introduction

Neuronal connections among cortical areas can be observed at a variety of scales in the brain, from laminar circuits to cortico-thalamic and cortico-cortical connections. Together they form a complex and intricate set of connections that serve as pathways for signal transmission and processing. The anatomy and function of such connections has been a focus of much research during the last decades (Biswal et al. 1995; Le Bihan et al. 2001;

Vincent et al. 2007). Thanks to noninvasive forms of neuronal recordings, like functional magnetic resonance imaging fMRI (Raichle 2000, for a detailed review), the link between structural and functional connectivity in the human brain has begun to be unraveled in vivo. However, due to the multiple physiological mechanisms contributing to the **blood-oxygen-level-dependent (**BOLD) signal (i.e., metabolic, vascular, neuronal, etc.), its limited temporal resolution, and high noise level in its measurements (Buzsáki et al. 2007; Tong et al. 2014), it is still difficult to quantify and interpret this relationship link using fMRI. Several strategies have been proposed to address these issues and infer the efficacy with which anatomical connections modulate interactions between brain regions—referred to as effective connectivity (EC) (Friston et al. 2003; Goebel et al. 2003; Penny et al. 2004; Cardin et al. 2011; Seth et al. 2015; Gilson et al. 2016). However, most such strategies rely on the assumption of temporal precedence: the temporal resolution of the BOLD signal and its measurement must be sufficient to capture the time scale of modulatory influences. Crucially, the observed responses should reflect temporal dependencies within the system under scrutiny, which may not be the case if hemodynamic response delays differ between regions (Aguirre et al. 1998; Harrison et al. 2002; Handwerker et al. 2004; Aquino et al. 2012).

The analysis of BOLD activity propagation is one of such approaches. It uses the spatiotemporal covariance structure (the zero-lag covariance and time-lag covariance) to infer propagated signal flows across different brain regions (Mitra et al. 2015). Interestingly, for whole-brain fMRI recordings, it has been recently shown that the temporal structure of BOLD signals is modulated across different behavioral states (Mitra et al. 2016). This suggests a meaningful relationship between BOLD activity propagation and the modulation of communication between distant brain regions. Therefore, we ask if the propagation of BOLD activity can also reveal modulation across different behavioral states at a more local scale, such as that of early cortical visual field maps, which are richly interconnected and where regional variation in the hemodynamic response is less pronounced (Handwerker et al. 2004; Lin et al. 2017).

In the present study, we hypothesize that the propagation of BOLD activity across early cortical visual field maps V1, V2, and V3 reflects structured neuronal activity (i.e., modulation of EC weights) within and between these maps. To examine this hypothesis, we implement a data-driven network model that captures the propagating nature of the BOLD signals (Gilson et al. 2016, 2018). This model aims to reproduce the BOLD spatio temporal covariance structure. It comprises three sets of parameters that interplay in generating the BOLD structure spatiotemporal structure: the EC, the nodal temporal decay, and the local (nodal) variability. Disentangling different possible origins of the observed lags is crucial for the interpretation of the BOLD data. This makes our approach better at capturing the cortical dynamics underlying BOLD signal flows than simpler lagged analyses that do not take into account the network constraints on the observed activity. Our model thus accounts for the spatiotemporal statistics of BOLD activity and thereby the propagation of BOLD activity across different brain locations (Gilson et al. 2016, 2018). We apply this approach to resting state (RS) and visual field mapping (VFM) fMRI recordings of the early cortical visual field maps V1, V2, and V3 in healthy human participants. To preview our results, in both RS and VFM data, we find a common structure underlying the EC of all participants, regardless of inter-participant variation in EC estimates. The common structure in EC links regions with similar visual field position selectivity both within and between early visual cortices (i.e., across both their topography and hierarchy). Furthermore, the estimated ECs capture different interaction regimes in RS and VFM. Within-area interactions, particularly in V1 and V3, are greatly increased in RS, whereas in VFM between area interactions are increased, particularly feedback interactions from V2 and V3 to V1. Moreover, local cortical excitability in V1 is increased during RS but, during VFM, decreases to levels that are comparable with that of other visual areas. These differences point to a change of input to V1 and appear to reflect a different configuration of feedforward, lateral and feedback interactions in rest (RS, eyes closed) and task (VFM). Finally, we interpret our results under the framework of predictive coding, emphasizing the role of recurrent cortical feedback during visual processing. Taken together, our results demonstrate that the propagation of BOLD activity through early visual cortices has functional relevance.

Materials and Methods

Data

The data comprise VFM and RS 7T fMRI data from eight healthy human participants (age 26–40) with normal visual acuity. Experimental procedures were approved by the medical ethics committee of the University Medical Center Utrecht.

VFM

Visual stimuli were presented by back-projection onto a 15.0×7.9-cm gamma-corrected screen inside the MRI bore. Participants viewed the display through prisms and mirrors, and the total distance from the participants eyes (in the scanner) to the display screen was 36 cm. Visible display resolution was 1024×538 pixels. The stimuli were generated in Matlab (Mathworks, Natick, MA, USA) using the PsychToolbox (Brainard 1997; Pelli 1997). The VFM paradigm consisted of drifting bar apertures at various orientations, which exposed a 100% contrast checkerboard moving parallel to the bar orientation. After each horizontal or vertical bar orientation pass, 30 s of mean-luminance stimulus was displayed. Throughout the VFM, participants fixated a dot in the center of the visual stimulus. The dot changed color between red and brown at random intervals. To ensure attention was maintained, participants pressed a button on a response box every time the color changed. Detailed procedures can be found in Dumoulin and Wandell (2008) and Harvey and Dumoulin (2011). The radius of the stimulation area covered 6.25° of eccentricity (visual angle from the fixation point).

RS

During the RS scans, the stimulus was replaced with a black screen and participants closed their eyes. The lights in the scanning room were off and blackout blinds removed light from outside the room. The room was in complete darkness. Thus, visual stimulation was minimized. The participants were instructed to think of nothing in particular without falling asleep.

fMRI Acquisition

Functional T2*-weighted 2D echo planar images were acquired on a 7-Tesla scanner (Philips, Best, Netherlands) using a 32-channel head coil at a voxel resolution of $1.98 \times 1.98 \times 2.00$, with a field of view of $190 \times 190 \times 50$ mm. TR was 1500 ms, TE was

25 ms, and flip angle was set to 80°. The volume orientation was approximately perpendicular to the calcarine sulcus. In total, eight 240 volumes of functional scans were acquired, comprising 5 RS scans interleaved with 3 VFM scans (first was an RS scan). Five dummy volumes were scanned before data acquisition began, and a further eight volumes were discarded from the beginning of each scan to ensure the signal had reached a steady state. High-resolution T1-weighted structural images were acquired at a resolution of $0.49 \times 0.49 \times 0.80$ mm (1 mm isotropic resolution for the second dataset), with a field of view of $252 \times 252 \times 190$ mm. TR was 7 ms, TE was 2.84 ms, and flip angle was 8°. We compensated for intensity gradients across the image using an MP2RAGE sequence, dividing the T1 by a co-acquired proton density scan of the same resolution, with a TR of 5.8 ms, TE of 2.84 ms, and a flip angle of 1°. Physiological recordings were not collected.

Preprocessing

First, the T1-weighted structural volumes were resampled to 1-mm isotropic voxel resolution. Gray and white matter were automatically labeled using Freesurfer, and labels were manually edited in ITKGray to minimize segmentation errors (Teo et al. 1997). The cortical surface was reconstructed at the white/gray matter boundary and rendered as a smoothed 3D mesh (Wandell et al. 2000). Head motion within and between scans was corrected using robust multiresolution alignment of MRI brain volumes (Nestares and Heeger 2000). Subsequently, data were aligned to the anatomical scans and interpolated to the anatomical segmentation space (Nestares and Heeger 2000). Instrumental drift was removed by detrending with a discrete cosine transform filter with a cutoff frequency of 0.01 Hz.

Selection of Regions of Interest

Since the focus of our study was modeling the propagation of BOLD activity within and between early visual field maps, we did not consider all recorded locations in the scanning volume. Instead, we applied a region of interest (ROI) selection and a data-reduction step. First, we identified the visual field maps of the visual cortical areas V1, V2, and V3 (see Population Receptive Field Modeling). Second, we grouped the BOLD signals over the foveal and parafoveal quarter fields of these maps. This resulted in a network of 24 nodes (ROIs) per participant (see Grouping of Data into Foveal and Parafoveal Quarter-fields).

Population Receptive Field Modeling

The visual field maps of V1, V2, and V3 were obtained using the population receptive field (pRF) method (Dumoulin and Wandell 2008) applied to our VFM data. This method provides models that summarize the visual field position to which each recording site responds as a circular Gaussian in visual space. The Gaussian pRF model for each recording site was characterized by three parameters: x and y (position) and size (sigma). These parameters were determined by taking a large set of candidate pRF parameters, with each set defining a different Gaussian. By quantifying the overlap between each candidate pRF Gaussian and the stimulus aperture at each time point, we generate predictions of the neuronal response time course each candidate pRF would produce. This predicted neuronal response time course is convolved with the hemodynamic response function (HRF) to give a set of candidate predicted fMRI response time courses for each candidate set of pRF parameters. In order to reduce the influence of high-frequency variation during pRF modeling, the detrended signals were filtered with a low-pass fourth-order Butterworth filter with a cutoff frequency of 0.1 Hz. The best fitting predicted fMRI time course and its associated pRF parameters are then taken to summarize the visual field selectivity of each recording site (Dumoulin and Wandell 2008). Recording sites were excluded from subsequent analyses if their best-fitting pRF models explained less than 30% of response variance, or had visual field eccentricities beyond 6°.

Grouping of Data into Foveal and Parafoveal Quarter-fields

We grouped the RS and the VFM time series over the foveal and parafoveal quarter fields of V1, V2, and V3 using the eccentricity and polar angle pRF preferences of each recording site. The foveal ROIs grouped recording sites with pRF positions below 2.2 degrees of eccentricity, while parafoveal ROIs grouped recording sites with pRF positions above 2.2 degrees of eccentricity. Quarter fields were divided at the vertical and horizontal visual field meridians using the pRF coordinates for the vertical and horizontal phase inversion in pRF polar angle (overlapping voxels between visual areas were excluded). The grouping process resulted in a matrix of 24 nodes/ROIs, 8 for each complete visual field map (V1, V2, and V3). Signals for each of the 24 ROIs were obtained by averaging the BOLD time series within the ROIs. No low-pass filtering was applied prior to this averaging step. However, voxels with BOLD amplitude variability greater than the third quartile were considered outliers and removed (Meehan et al. 2017). This allowed EC estimates to capture high frequencies in the BOLD signals (close to the Nyquist frequency for the BOLD data, 0.33 Hz), while excluding high-variance fluctuations, likely from vascular origin (Winawer et al. 2010).

EC Model for BOLD Propagation

In this section, we examine the propagation of BOLD activity across the foveal and parafoveal quarter fields of V1, V2, and V3 (each of the 24 ROIs previously defined) using a recently proposed method (Gilson et al. 2016). This approach uses a noise-diffusion network model of EC and intrinsic variability to account for local BOLD variability and signal propagation lags between all possible pairs of ROIs. Importantly, the model captures the empirical data covariance and its spatio-*temporal* structure (the time-shifted covariances), effectively accounting for the propagation of BOLD activity. This has the advantage of relying on minimal assumptions: 1) the time constant of the generative model has to match the autocovariance time constant derived empirically from the data, 2) the regional variation in the hemodynamic response shape across early visual cortex should be minimal (Handwerker et al. 2004; Lin et al. 2017), and 3) for each behavioral condition, a dominant pattern of neuronal interactions should influence and reflect in the average propagation structure of the BOLD signals. To examine our hypothesis (BOLD activity propagation reflects the consequences of structured neuronal activity), we model the EC under two conditions: 1) RS and 2) the presentation of VFM stimulus, and compare the two. We iteratively tune the model parameters (directed connectivity with notation C and intrinsic variability with notation Σ and) to reproduce the empirical spatiotemporal covariance and then use the C and Σ associated with the best-fitting model as an estimate of the EC and the local cortical excitability of the actual data. We conclude comparing the resulting differences in EC and cortical excitability between RS and VFM.

Empirical Spatiotemporal Covariances

To identify the spatiotemporal covariance structure of the data (the BOLD signals from each of the 24 ROIs; see Methods), we estimated the covariance with and without time shifts. For each participant and condition, the BOLD signals were first demeaned and then, following Gilson et al. (2016), the empirical covariance was calculated for zero lag:

$$\hat{Q}^0_{ij} = \frac{1}{T-2}\sum\nolimits_{1\le t\le T-1}\left(s^t_i - \overline{s_i}\right)\left(s^t_j - \overline{s_j}\right), \quad (1)$$

and a lag of 1 TR:

$$\hat{Q}^1_{ij} = \frac{1}{T-2}\sum\nolimits_{1\le t\le T-1}\left(s^t_i - \overline{s_i}\right)\left(s^{t+1}_j - \overline{s_j}\right). \quad (2)$$

Here, $\overline{s_i}$ is the mean BOLD level over the session for ROI i. Afterwards, for each participant and session, we estimated the empirical time constant associated with the exponential decay of the autocovariance (averaged over all regions):

$$\tau = \frac{N}{\sum_{1\le i\le N}\log\left(\hat{Q}^0_{ii}\right) - \log\left(\hat{Q}^1_{ii}\right)} \quad (3)$$

The time constant τ was used to calibrate the noise-diffusion network model.

Noise-diffusion Network Model of EC and Parameter Estimation

We choose a dynamic network model that captures the spatiotemporal dynamics of the data. Here, we summarize the essential ingredients of the model and its optimization (for further details see Gilson et al. (2016, 2018)). The model consists of 24 interconnected nodes (as defined in Selection of Regions of Interest) that experience fluctuating activity and excite each other (Gilson et al. 2016). The local variability is described for each node by a variance corresponding to the diagonal term of the matrix Σ. The implicated fluctuations are shaped by the network EC (denoted by the matrix C in the following equations) to generate the model FC, which is quantified the zero-lag covariance matrix Q^0 (FC0) and the time-lag covariance matrix Q^1 (FC1) (the counterparts of the empirical $\hat{Q}^0$ and $\hat{Q}^1$). Subsequently, the model covariance matrices Q^0 and Q^1 that better reproduce the empirical spatiotemporal covariances $\hat{Q}^0$ and $\hat{Q}^1$ are approximated by iteratively adjusting the directional weights (C) and node excitabilities (Σ) of the model using Lyapunov optimization (LO) to reduce the model error E (specified later in Eq. (8)). The parameters C and Σ associated with the best-fitting model correspond to maximum-likelihood estimates (Gilson et al. 2016). Importantly, because asymmetry in the C_{ij} generates asymmetry in the time-shifted covariances Q^1, the model captures the average propagation structure between ROIs.

We choose LO because it has several advantages to other methods (Gilson et al. 2016): 1) pairwise unconditional Granger causality does not take the whole network into account, 2) multivariate autoregressive models that take the whole network into account may suffer from the down sampling due to the time resolution (TR = 1.5 s), and 3) physical interpretability might be hindered by over-parameterized dynamic causal models (Goebel et al. 2003; Harrison et al. 2003; Smith et al. 2011). These advantages allowed us to estimate C_{ij} (and the corresponding asymmetry in Q^1) and Σ as accurately as possible. Our approach was also justified because the decay time constant τ in Eq. (3) was consistently measured across participants, suggesting a diffusion process in the empirical data; the goal of our model inversion was then to examine whether propagation was present in the data. Now, we detail the equations relating these parameters, observables and measures. Formally, the network model is a multivariate Ornstein–Uhlenbeck process where the activity x_i of node i decays exponentially with the time constant τ estimated from the data in Eq. (3). The evolution of each x_i depends on the activity of other populations and the local variability:

$$dx^t_i = \left(-\frac{x^t_i}{\tau} + \sum\nolimits_{j\ne 1} C_{ij}x^t_j\right)dt + dB_i, \quad (4)$$

where dB_i is — both spatially and temporally — independent Gaussian noise with variance Σ_{ii} (the Σ matrix is diagonal); formally B_i a Wiener process. The model Q^0 can be calculated for known C and Σ by solving the Lyapunov equation (using the Bartels–Stewart algorithm):

$$JQ^0 + Q^0J^\dagger + \Sigma = 0 \quad (5)$$

and Q^1 is then given by

$$Q^1 = Q^0\mathrm{expm}\left(J^\dagger\right), \quad (6)$$

where expm denotes the matrix exponential, the superscript † indicates the matrix transpose, and δ_{ij} is the Kronecker delta. In those equations, the Jacobian J of the dynamic system is defined as

$$J_{ij} = -\frac{\delta_{ij}}{\tau} + C_{ij}. \quad (7)$$

Equations (5) and (6) enable the quick calculation of Q^0 and Q^1, without simulating the network activity. The LO starts with zero connectivity ($C = 0$) and uniform local variances ($\Sigma_{ii} = 1$). Each iteration of LO aims to reduce the model error defined as

$$E(C,\Sigma) = \frac{\left\|\Delta Q^0\right\|^2}{\left\|\hat{Q}^0\right\|^2} + \frac{\left\|\Delta Q^1\right\|^2}{\left\|\hat{Q}^1\right\|^2}, \quad (8)$$

with the difference matrices $\Delta Q^0 = \hat{Q}^0 - Q^0$ and $\Delta Q^1 = \hat{Q}^1 - Q^1$; the vertical bars $\|\cdot\|$ indicate the Frobenius norm. To do so, we calculate the model Q^0 and Q^1 for the current values of the parameters C and Σ by solving Eqs (5) and (6). Similar to a gradient descent, the Jacobian update is given by:

$$\Delta J^\dagger = \left(Q^0\right)^{-1}\left[\Delta Q^0 + \Delta Q^1\mathrm{expm}\left(J^\dagger\right)\right], \quad (9)$$

which gives the connectivity update:

$$\Delta C_{ij} = \eta_C \Delta J_{ij}. \quad (10)$$

where η_C is the optimization rate of C (here we $\eta_C = 0.0001$). To take properly the network effects in the Σ update, we adjust the

Σ update from the heuristic update in Gilson et al. (2016) as was done in Gilson et al. (2018):

$$\Delta\Sigma = -\eta_\Sigma \left(J\Delta Q^0 + \Delta Q^0 J^\dagger \right). \quad (11)$$

where η_Σ is the optimization rate of Σ (here $\eta_\Sigma = 1$). We impose non-negativity both for C and Σ. In addition, off-diagonal elements of Σ are kept equal to 0 at all times. The optimization steps are repeated until reaching a minimum for the model error E, giving the best fit and the model estimates. The C and Σ associated with the best predicting model are then taken as a proxy for the EC between the 24 ROIs and their local cortical excitability (Σ).

To facilitate comparison between RS and VFM, the resulting Σ values were further grouped across foveal and parafoveal ROIs in each hemisphere (giving a total of 6 new ROIs). A similar approach was applied to the resulting C_{ij} values (see the next section).

Determination of Common Underlying Structure in EC and Its Relation to Topographic and Anatomical Connectivity

Due to the nature of the model parameter estimation, the estimated EC weights can incidentally vary in magnitude across participants (reflecting session-to-session variability, subject heterogeneity, etc.). However, the ranking of the EC weights may be more invariant and reveal a structure in the EC that is common to all participants. To identify this common structure, in RS and in VFM, we proceed as follows. First, the raw EC estimates are normalized by dividing the EC weights by their L1-norm (the sum of the EC weights in the considered matrix). This process renders individual EC estimates comparable across participants (magnitudes are normalized but rank is preserved). Second, we quantify the stability of the EC estimates using a test–retest procedure: 1) we randomly split the normalized EC in to two halves, 2) average each half, and then 3) compute the Pearson correlation between all the possible EC averages ($8!/4!/4! = 70$). We use the correlation coefficients thus obtained to summarize the stability of the EC estimation for each condition. Subsequently, we use principal component analysis (PCA) to detect the common structures. Intra- and interhemispheric EC values were z-scored and PCA applied separately and the highest 10% of the first principal component was taken as a proxy for the common inter- and intrahemispheric EC structures. We justify this step because applying PCA to a mix of strong intrahemispheric EC links and weak long-range callosal interhemispheric EC links may hinder the detection of each class separately (Stephan 2005). Separating these classes manually enabled the detection of the underlying structure in the ranking of the component, regardless of the difference in the EC magnitudes between the two types of connection. We then went on to examine differences in EC between RS and VFM. To summarize EC interactions and facilitate comparison between conditions, we applied a data reduction step: for each condition and participant, the normalized EC values that matched the common structure were grouped into foveal and parafoveal regions of V1, V2, and V3 and averaged across these visual field maps. This allowed us to focus on foveal/parafoveal differences. The reduced individual EC matrices were z-scored, and significant differences between the VFM- and RS- derived EC were evaluated using permutations corrected for multiple comparisons (Nichols and Holmes 2001).

Results

Propagation of BOLD Activity Across Early Visual Cortex Measured with a Noise-diffusion Network Model of EC

Figure 1 illustrates the propagation of an apparent wave of BOLD activity from the anterior calcarine sulcus (periphery of V1) to the occipital pole (foveal confluence of V1, V2, and V3) during rest (RS). To estimate the propagation of BOLD activity across early visual cortex, we first obtained visual field maps of V1, V2, and V3 using the pRF method (Fig. 2A). We then further subdivided these maps into foveal and parafoveal (below and above 2.2 degrees of eccentricity) quarter fields (see Selection of Regions of Interest). This provided us with a functional map of the cortex based on similarities in both retinotopy and hierarchy. Second, we characterized BOLD activity propagation patterns during RS and VFM through V1, V2, and V3 using a data-driven modeling approach (see EC Model for BOLD Propagation). Here, we used the temporal autocovariance constant derived empirically from the data to calibrate a topologically agnostic (unconstrained by anatomical connections) noise-diffusion network model of EC and cortical excitability. Figure 2B presents the results from the analysis of the temporal autocovariance. Although the time constant (τ, in seconds) was slightly lower in RS than in VFM (mean (standard deviation, SD) = 5.49 (2.96) for RS and 6.32 (1.30) for VFM), this difference was not significant, suggesting similar propagation time scales. Note that the propagation pattern illustrated in Figure 1 unfolds within the range measured by the autocovariance decay constant.

We then modeled the spatiotemporal covariance structure of the data by optimizing the noise-diffusion network parameters, namely the EC and the nodes excitabilities (Σ), to reproduce the empirical spatiotemporal covariances FC0 and FC1. Figure 2C illustrates one iteration step in the LO procedure used to solve the model. The goodness of fit between the modeled and empirical spatiotemporal covariances was computed using the linear regression coefficient R^2 between the modeled and the empirical FC0 and FC1 (see Table 1).

Common Underlying Structures in EC

We then asked if there was a common structure underlying the resulting EC distribution. Regardless of individual variations in EC values obtained from RS and VFM data (Fig. 3A), our analysis revealed a common underlying structure for both RS and VFM (Fig. 3B). Figure 3A compares the similarity between EC links in a test–retest validation with split-halves (see Determination of Common Underlying Structure in EC and Its Relation to Topographic and Anatomical Connectivity for details). The similarity is measured by the Pearson correlation coefficient between average ECs from all possible combinations: mean (SD): 0.9439 (0.0026) for VFM and 0.839 (0.0676) for RS). These results indicate a similar EC structure, or hierarchy defined by the relative pairwise differences, that generalize across subjects for each condition (RS or VFM). Figure 3B illustrates the common structure in EC as green crosses overlaid onto the grand average EC for RS and VFM. The common structures in EC closely matched the homotopy and hierarchy of the underlying anatomical connections. This agrees with recent reports indicating that resting-state fMRI activity closely reflects the anatomical organization of the visual cortex both with respect to retinotopy and hierarchy (Heinzle et al. 2011; Gravel et al. 2014; Gençet al. 2016). Our results further indicate that the homotopic organization is even more precisely captured in VFM than in RS. This goes together with an increased stability of ECs across subjects in VFM.

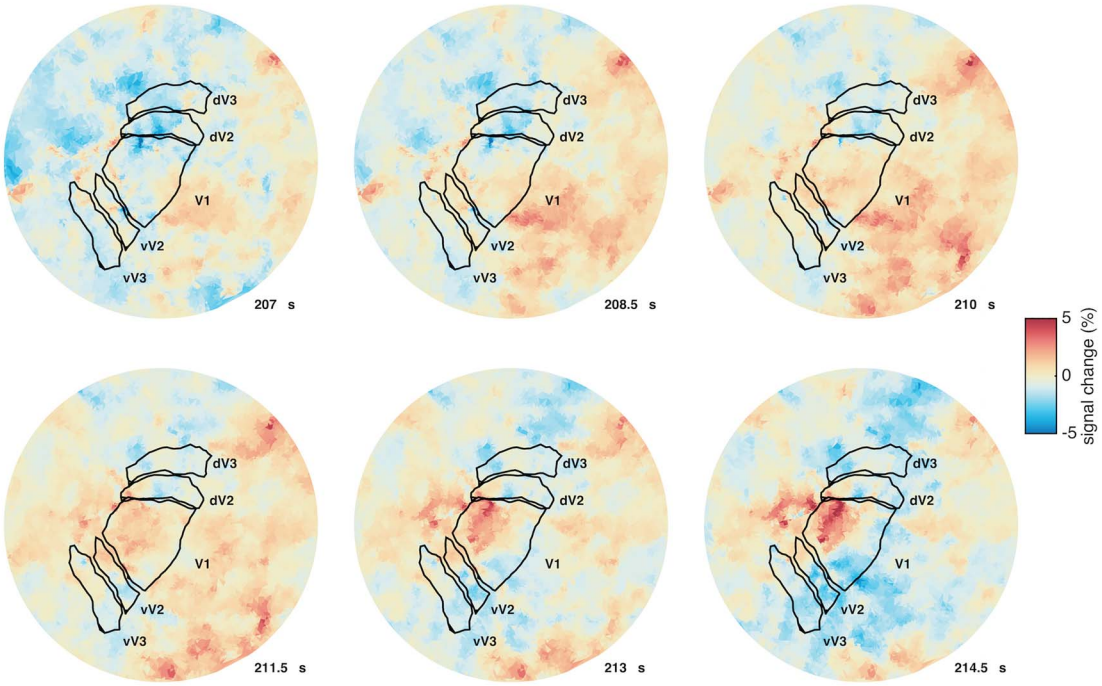

Figure 1. Apparent propagation of BOLD activity during RS depicted in the flattened cortical surface reconstruction of the occipital pole of one participant's cerebral hemisphere. Early visual field maps V1, V2, and V3 in one hemisphere are outlined in black (d and v denote dorsal and ventral). In the absence of visual stimulation (i.e., eyes closed, total darkness), spontaneous fluctuations in BOLD activity (indicated by the hot and cold colors) during RS can exhibit extensive spatiotemporal structure. This structure includes spatiotemporal fluctuation patterns that resemble stimulus-evoked waves as well as congruent and transient co-activations that occur across the visual field maps. Note that the analytical model used to describe this structure directly reproduces the empirical spatiotemporal covariance of the data and does not simulate the BOLD time series. In other words, the model aims to capture the mean propagation of the BOLD waves shown here, averaged over each fMRI session. The narrow time window was used to illustrate a single propagation event.

Differences in EC and Σ between RS and VFM

We then went on to examine the topology of the resulting common structures in EC and their differences between conditions. Figure 4 illustrates the common structures in EC (lateral and callosal, feedforward and feedback interactions) across the foveal and parafoveal quarter fields of the visual field maps for RS and VFM. In both conditions, intra- and interhemispheric connections linked regions with similar visual field selectivity. However, in VFM, interhemispheric connections linked foveal regions only, whereas in RS, interhemispheric connections linked also parafoveal regions, mostly in V1. Both in RS and VFM, feedback connections outnumbered feedforward connections (Fig. 4).

Subsequently, to interpret changes in the EC and cortical excitability between RS and VFM, we grouped the corresponding EC and Σ values across the four quadrants in each visual field map to give foveal and parafoveal regions of each visual field map (the six ROIs defined in Noise-diffusion Network Model of EC and Parameter Estimation). We then evaluated differences in EC between the two conditions across participants using permutations corrected for multiple comparisons (with a significance threshold of $P < 0.05$). Figure 5A illustrates the resulting ECs and the differences between conditions (VFM-derived EC – RS-derived EC). These results show that strong interactions within V1 and V3 in RS are absent in VFM. Conversely, feedforward interactions between V1 and V2 were present only in VFM, whereas feedforward interactions between V2 and V3 were present both in RS and VFM, although foveal interactions were increased for VFM.

Furthermore, feedback interactions between V2 and V1 and V3 and V2 were present both in RS and VFM, although feedback interactions between V3 fovea and V2 fovea were greatly increased in VFM. Notably, homotopic feedback interactions between V3 and V1 were only detected in VFM. Figure 5B illustrates the cortical excitability parameter Σ in RS and VFM. Changes were most pronounced in V1, with higher values of Σ in foveal regions for RS and parafoveal regions for VFM. Differences were not significant.

Discussion

We assessed the propagation of BOLD activity through early visual cortical areas V1, V2, and V3 during RS and VFM using a data-driven modeling approach based on a noise-diffusion network model. Informed by the empirical spatiotemporal covariance structure of BOLD co-fluctuations within and between visual cortical areas, this model estimates a topologically agnostic (unconstrained by anatomical connections) EC. Our model decomposes the spatiotemporal structure of BOLD fluctuations into an EC parameter and a local cortical excitability parameter Σ. Importantly, the combination of the estimated parameters explain the temporal lags between BOLD signals from all pairs of ROIs, effectively accounting for observed propagation in the data. This discussion comprises four sections. In the first section, we examine the neuroanatomical substrate and the possible mechanisms implicated by the different EC interactions estimated for RS and VFM. Our focus here is to emphasize the role of recurrent feedback connectivity and

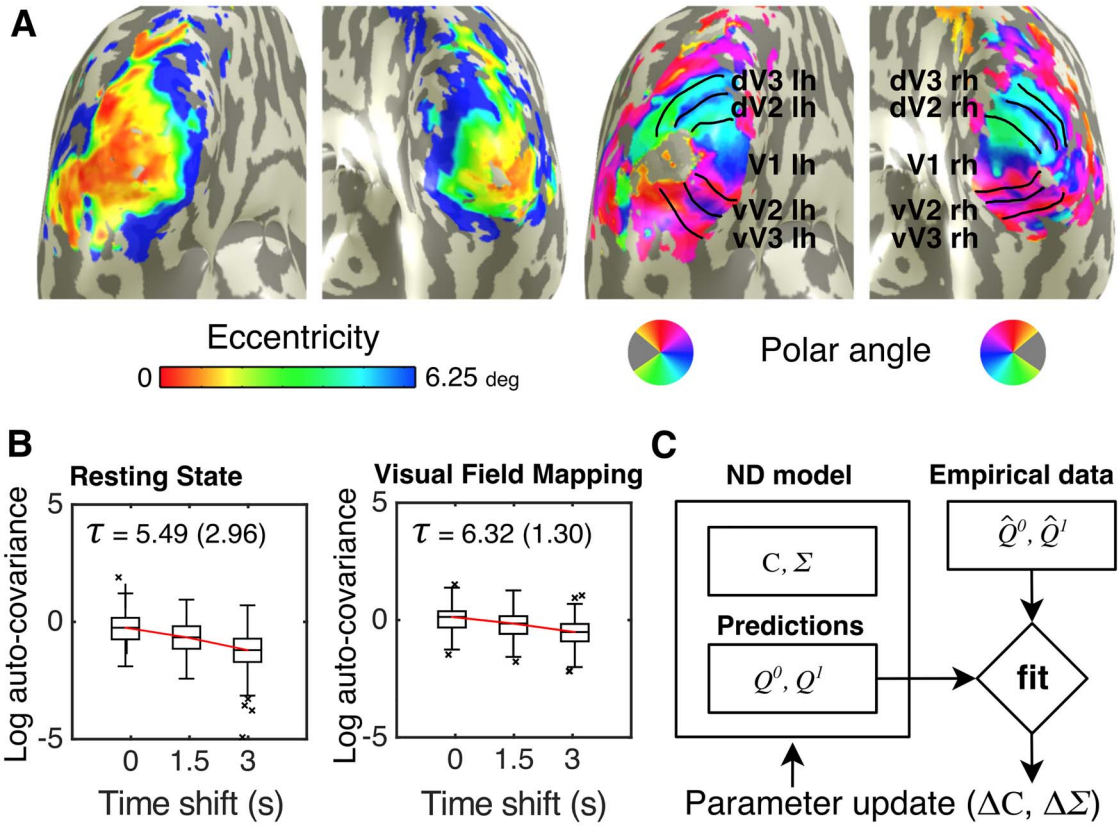

Figure 2. Modeling the propagation of BOLD activity across visual field maps V1, V2, and V3. (*A*) Visual field maps in striate (V1) and extrastriate cortex (V2 and V3) were mapped using the pRF modeling method (Dumoulin and Wandell 2008). Based on the visual field position, selectivity estimates that the pRF method provides and is further subdivided into foveal (below 2.2 degrees of eccentricity) and parafoveal (between 2.2 and 6 degrees of eccentricity) quarter fields in both hemispheres, giving a total of 24 ROIs (see Selection of Regions of Interest). A threshold of 10% variance explained was applied to pRF maps. The gray region in the foveal confluence of the left hemisphere's occipital pole is gray because of the colormap limited coloring of the ipsilateral visual field (gray area in the color wheel). We used a noise-diffusion network model of EC to estimate the propagation of BOLD activity and the cortical excitability across these foveal and parafoveal quarter fields of V1, V2, and V3. (*B*) Logarithm of the autocovariance of the BOLD activity, averaged across participants and ROIs, as a function of the time shift (*x*-axis). The red lines link the mean of each box plot. The time constant τ was calculated for each participant and condition (see Empirical Spatiotemporal Covariances). The mean (SD) of τ over all participants is indicated above the box plots. The empirical time constants were used to calibrate the noise-diffusion network model. (*C*) Schematic diagram illustrating one step in the LO procedure. By iteratively adjusting the connectivity C and node excitability Σ of the noise-diffusion network, the model spatiotemporal covariance (Q^0, Q^1) approximates the empirical spatiotemporal covariance ($\hat{Q}^0$, $\hat{Q}^1$). For each participant and condition, the C and Σ corresponding to the best predicting model were taken as estimates of the underlying EC and the local cortical excitability.

non-stimulus-driven inputs, as well as examine the functional implications of our findings from a theoretical perspective, touching upon the notion of predictive coding (Rao and Ballard 1999; Lee and Mumford 2003). In the second section, we discuss the possible mechanisms that underlie the changes in cortical excitability (Σ) observed between RS and VFM and relate those to changes in EC. In the third section, we relate the BOLD autocovariance decay constant to different behavioral states. In the last section, we discuss the methodological and theoretical limitations of our study and raise questions for future research.

Recurrent Connectivity and Its Role in Visual Processing

We demonstrate that the propagation of BOLD activity across the topography and hierarchy of (i.e., within and between) visual field maps V1, V2, and V3 reveals different directed interaction regimes for RS and VFM (Fig. 3). We relate these differences in EC to a task-dependent reconfiguration of lateral, feedforward and feedback interactions (Fig. 4). Across visual field maps, feedforward EC interactions from V1 to V2 were found in VFM but not in RS. However, later in the hierarchy, feedforward interactions from V2 to V3 were observed both in RS and VFM, though foveal interactions were increased in VFM (Fig. 5A). We attribute these increased feedforward interactions during VFM, both from V1 to V2, and from V2 to V3, to stimulus-induced changes in neuronal pathways that increase the bottom-up processing of the stimulus across the visual hierarchy while participants are fixating on the screen. Furthermore, homotopic feedback interactions from V2 to V1 and from V3 to V2 were observed both in RS and VFM, although foveal interactions from V3 to V1 were greatly increased in VFM, again pointing to changes driven by the fixation task. This is consistent with previous findings showing a dissociation in functional coupling patterns between stimulus-driven versus surround regions of primary visual cortex (Haynes et al. 2005) during decreased stimulus visibility and top–down flow of visual spatial attention signals from parietal and temporal regions (Lauritzen et al. 2009; Al-Aidroos et al. 2012). Remarkably, homotopic feedback interactions from V3 to V1 were only observed for VFM (Fig. 5A), evidencing the role of extra-striate feedback in visual cortical processing (Gilbert and Li 2013).

Table 1 The goodness of fit between modeled and empirical spatiotemporal covariances

	RS		VFM	
Participant	FC0	FC1	FC0	FC1
1	0.646	0.625	0.694	0.655
2	0.471	0.330	0.704	0.690
3	0.884	0.824	0.710	0.670
4	0.880	0.878	0.756	0.733
5	0.888	0.858	0.674	0.611
6	0.871	0.837	0.705	0.654
7	0.972	0.956	0.731	0.707
8	0.842	0.820	0.755	0.709
Mean (SD):	0.81 (0.16)	0.76 (0.19)	0.72 (0.03)	0.67 (0.04)

Note: For each participant and condition, we evaluated the goodness of fit by computing the linear regression (R^2, $P < 10–50$ for all cases) between the modeled and the empirical spatiotemporal covariances (FC0 and FC1).

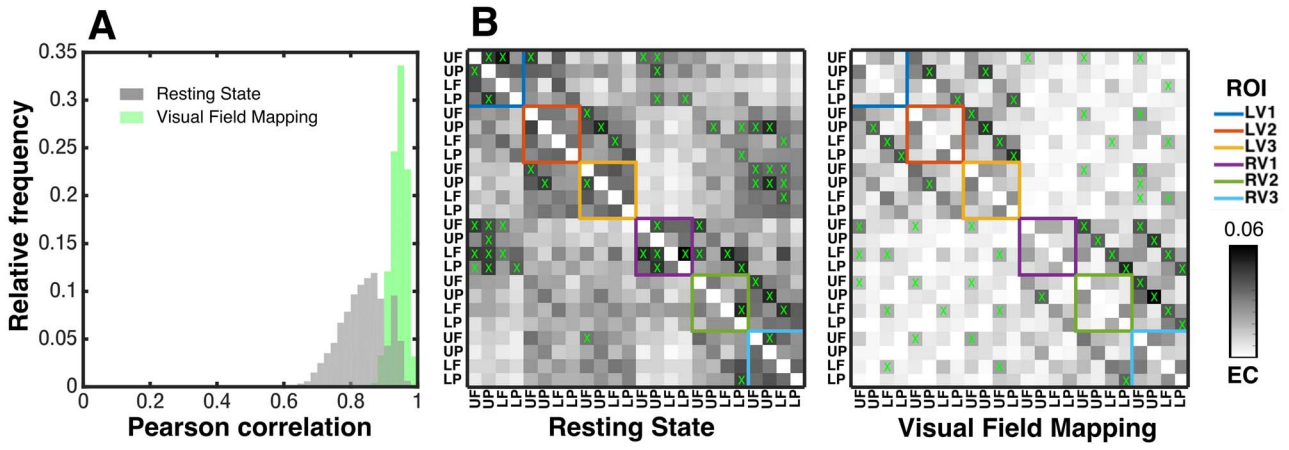

Figure 3. Stable patterns of EC in RS and VFM. (*A*) EC stability in RS and VFM. For each condition, EC stability across subjects was quantified using split-halves cross validation. Correlation coefficients are represented as relative frequency histograms (mean (SD) = 0.9439 (0.0026) for VFM and 0.839 (0.0676)). The similarity between individual ECs, as measured by the Pearson's correlation coefficient, was less stable in RS (two-sample *t*-test: $P < 10–10$). (*B*) Grand average EC for RS and VFM. The green crosses indicate the common structures detected with PCA. Diagonal and off-diagonal quadrants in each matrix represent within- and between- hemisphere EC across visual cortical areas (grouped by the colors), respectively. Inside each colored box, quarter fields are grouped in the following order (from left to right): upper fovea, upper parafovea, lower fovea, and lower parafovea. For each diagonal and off-diagonal quadrant, the upper triangle represents feedback connections and the lower triangle feedforward connections (rows correspond to inputs and columns correspond to outputs). Dark pixels represent stronger EC weights and white pixels weaker EC weights, as indicated by the colorbar.

At the level of individual visual field maps, we found directed EC interactions from the parafoveal to the foveal representations of V1 and V3 in RS but not in VFM. In principle, these interactions may reflect a bias in the spontaneous propagation of correlated neuronal activity along networks of functionally coupled regions and gradients of anatomically connected pathways or "connectopies," such as the eccentricity map in the calcarine sulcus (Yeo et al. 2011; Gençet al. 2016; Haak et al. 2017). This spontaneous propagation of correlated neuronal activity may presumably reflect intrinsic fluctuations in the ratio between excitation and inhibition and the modulation of lateral inhibitory coupling, known to give rise to spontaneous wave propagation patterns (Ermentrout and Cowan 1979; Heitmann and Ermentrout 2015). One interesting possibility is that these parafovea-to-fovea interactions reflect large-scale cortical waves traveling in the frontal-to-occipital direction. Slow-waves <1-Hz waves propagating in an antero-posterior direction during sleep and calmness (Massimini et al. 2004; Matsui et al. 2016) have been reported and may have a functional relevance (Jadhav et al. 2012; Logothetis et al. 2012; Kaplan et al. 2016). Our results echo and extend on a recent report showing an association between the integration of task-positive and task-negative networks and waves propagating towards the fovea during RS (Hindriks et al. 2019). During RS, intrinsic variation in input changes, such as the restructuring of corticothalamic network activity during wakeful detachment from the environment, might adjust the balance between excitation and inhibition in cortical neuronal populations in a state-dependent way (Steriade 2000). In the absence of stimulation, the increased parafovea-to-fovea EC interactions may well reflect visual cortical operations related to memory consolidation and learning (Mitra et al. 2016).

On the other hand, the absence of parafovea-to-fovea interactions during VFM can be explained by the stimulus set. Since the VFM stimuli consisted of a bar drifting at various orientations, the direction of neuronal response propagation may be balanced out and not reflected in EC estimates, which capture average propagation patterns only. Another line of evidence points to feedback modulation by top–down processes associated with attention and the predictability of a given

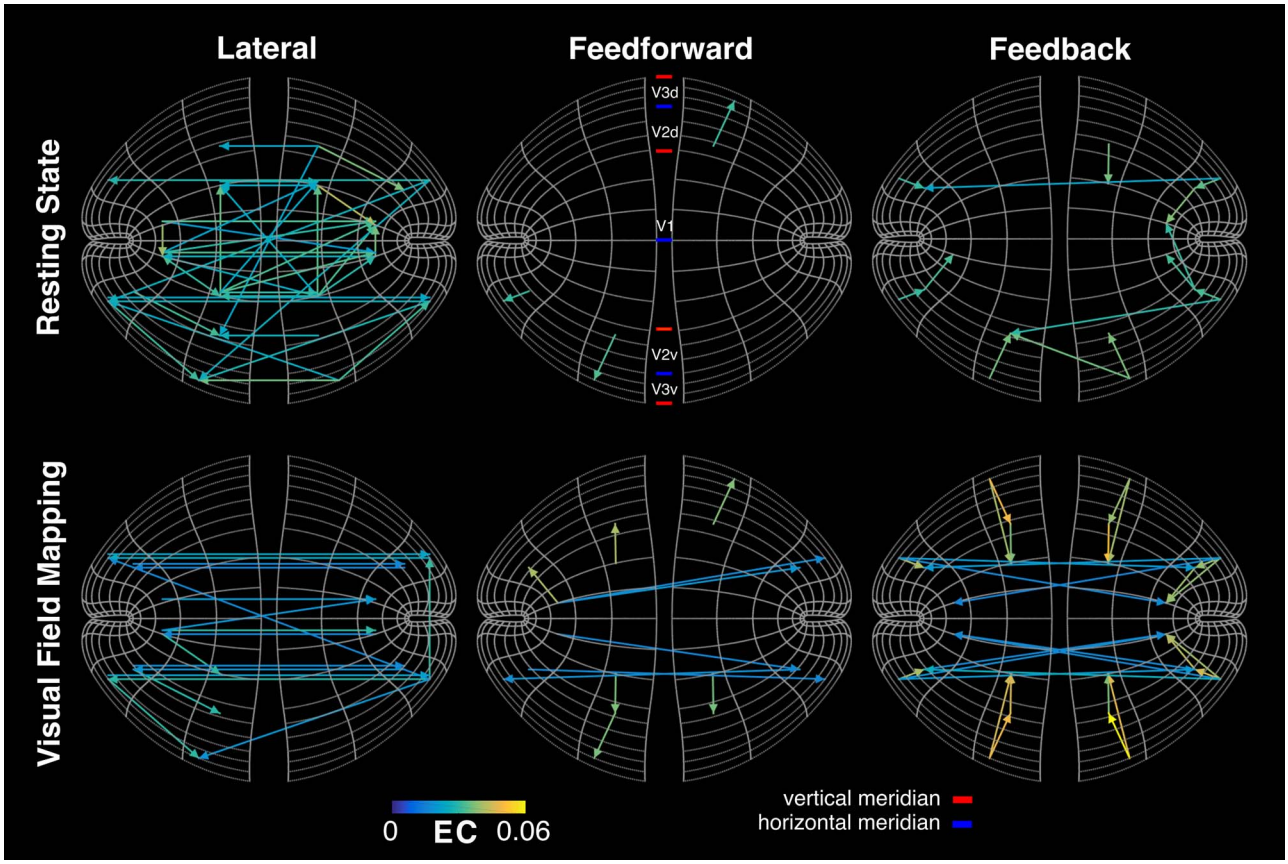

Figure 4. Common structure in EC for RS and VFM illustrated in visual cortical space. To facilitate the visualization of the lateral, feedforward, and feedback elements of the 24 ROIs EC network, we depict the common structures in EC between the 24 ROIs onto the banded 2D model of visual cortical areas V1, V2, and V3 as proposed Schira et al. (2010). Lateral (within ROIs), feedforward and feedback interactions are depicted as colored arrows. Colors depict the strengths of the grand average ECs. Colormaps for polar angle and eccentricity are illustrated by the miniature models in the bottom right corner (eccentricity range is 0–6°). The EC networks thus depicted reveal different interaction regimes in EC for RS and VFM.

stimulus (Kastner et al. 1999). Previous studies have suggested that predictable stimuli (e.g., drifting bars) induce less neuronal activity in early visual cortical areas than unpredictable stimuli (e.g., randomly changing dots) (Braddick et al. 2001; Harrison et al. 2007). Concomitantly, this reduced neuronal activity induced by predictable stimuli has been shown to result in suppressed BOLD responses in early visual cortex (Schellekens et al. 2016; Schindler and Bartels 2017). We note, however, that the attentional task used to ensure extended fixation during VFM may contribute with an unpredictable component to the VFM stimuli. The task consisted on fixating on a dot that changed colors randomly while, at the same time, pressing a button at the onset of every color change (Gilbert and Wiesel 1992; Vinje and Gallant 2000; Peter et al. 2019).

These results can also be interpreted within a predictive inference framework (Von Helmholtz 1867; Mumford 1994; Dayan et al. 1995; Lee and Mumford 2003). In this framework, recurrent feedforward/feedback loops serve to integrate top–down contextual priors (predictions) and bottom–up visual input by implementing a convergent probabilistic inference along the visual hierarchy. A relevant metaphor to understand this is the Helmholtz machine of Dayan et al. (1995) during perception, a top–down internal generative model learns to better reconstruct the input, whereas during rest, a bottom–up recognition model learns to refine internal representations that the generative model "dreams" (Dayan et al. 1995). From this perspective, the increased feedback to V1 and V2 observed for VFM might be interpreted as the dampening of feedforward visual responses according to prediction errors originated by the mismatch between incoming signals and internally generated top–down priors (Dayan et al. 1995; Rao and Ballard 1999; Lee and Mumford 2003; Friston 2005; Friston et al. 2006; Petro and Muckli 2016; Revina et al. 2017).

Cortical Excitability: Possible Mechanisms

Cortical excitability in RS, as quantified by Σ, was more variable than during VFM and was increased in V1, particularly in foveal representations (Fig. 5B). These differences in cortical excitability between foveal and parafoveal regions, although not consistently reaching statistical significance, may still have functional implications. Interestingly, this increase in cortical excitability was accompanied by strong directed interactions in EC from the parafovea to the fovea of V1 that were absent in VFM (Fig. 5A). One possibility is that these differences are related to changes in the power of occipital alpha oscillations, known to increase during wakeful detachment from the environment (i.e., RS) (Williamson et al. 1997; Harvey et al. 2013). If changes in the power of occipital alpha oscillations are partly captured by Σ, reduced cortical excitability in foveal regions of V1 could be

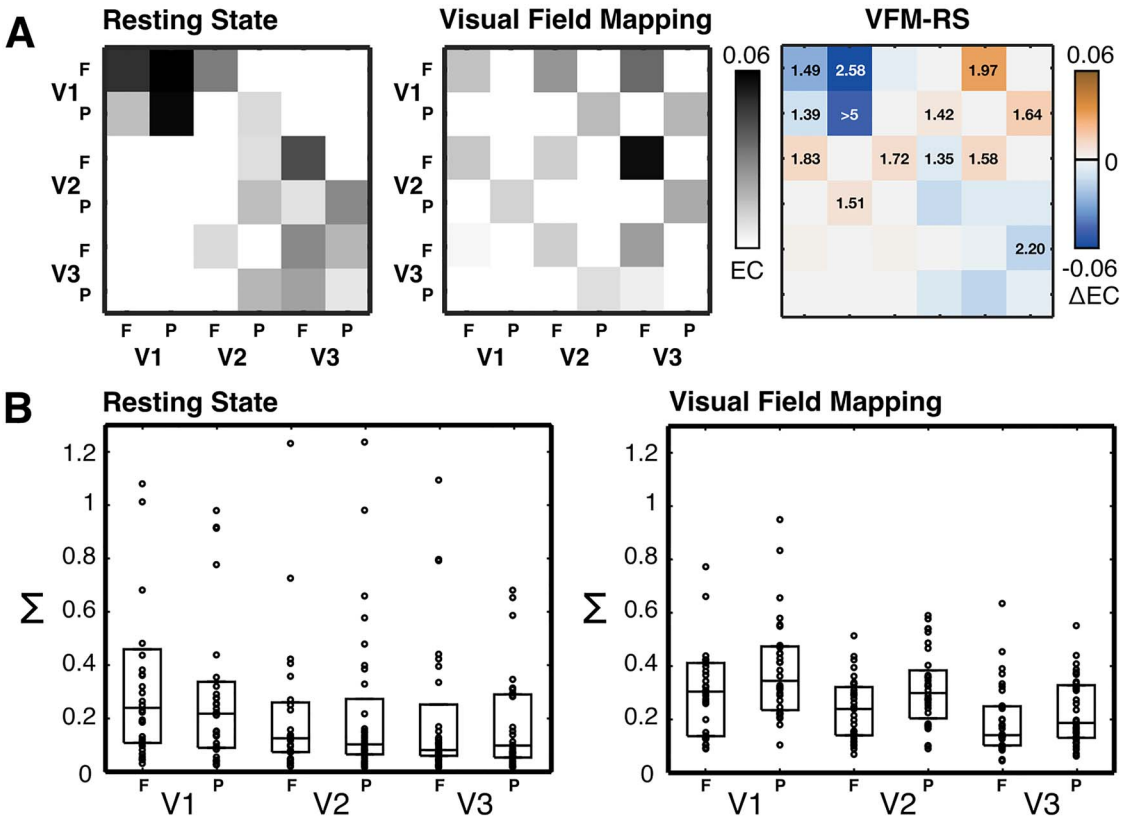

Figure 5. Differences in EC and Σ between RS and VFM suggest a reconfiguration of feedforward and feedback interactions. (*A*) Average EC matrices for RS (left panel) and VFM (middle panel) obtained by grouping significant EC links into foveal and parafoveal regions V1, V2, and V3 (F and P stand for fovea and parafovea. Columns represent output and rows inputs. See Determination of Common Underlying Structure in EC and Its Relation to Topographic and Anatomical Connectivity for details). The right panel illustrates the differences in EC between conditions (VFM-derived EC − RS-derived EC). Negative differences in EC (RS > VFM) are distinguished by a minus symbol mark in the upper left corner of the cell. Cells corresponding to regions that showed significant changes in EC (significant differences were evaluated using permutations corrected for multiple comparisons ($P < 0.05$)) have annotated the negative logarithm of their *P*-value ($-\log^{10}(P)$, note that $-\log^{10}(0.05) = 1.3$). Feedback connections outweighed feedforward connections both in RS and VFM. (*B*) Cortical excitability as estimated by Σ. For each condition, individual Σ estimates were grouped into foveal (F) and parafoveal (P) regions (as in A) and represented as black dots overlaid on box plots (the central mark is the median and the edges the 25th and 75th percentiles). A comparison between RS and VFM reveals a slight decrease in this value, particularly for foveal regions, albeit not significant. In VFM, Σ is slightly increased in the parafovea, although not significantly.

interpreted as reflecting surround suppression and facilitation in the fovea, while participants are fixating on the screen (Haegens et al. 2011; Harvey et al. 2013). Indeed, during a visual task, alpha oscillations in V1 have been associated with increased negative BOLD responses and shown to vary as a function of stimulus position and local receptive field surround (Harvey et al. 2013). The highly localized nature of these oscillations points to a role of intracortical axons in surround suppression (Schwabe et al., 2006, 2010; Harvey et al. 2013; Hindriks et al. 2014). In line with these studies, changes in Σ were identified in the foveal representation of V1 but not in extrastriate areas V2 and V3, likely reflecting the localized nature of occipital alpha oscillations. As discussed in Recurrent Connectivity and its Role in Visual Processing, extrastriate feedback to V1 may play a role modulating the balance between inhibition and excitation, known to change between task and rest, thereby reflecting differently in the BOLD signal during RS and VFM (Lamme et al. 1998; Petro et al. 2014). In the absence of visual input (RS), changes in cortico-cortical connectivity may leave V1 in a 'baseline' state of potential excitation, whereas during VFM, both external visual input and top–down feedback influences may modulate the balance between inhibition and excitation resulting in suppressed BOLD responses in V1 —thus attenuating cortical excitability (Angelucci and Bressloff 2006; Schellekens et al. 2016; Schindler and Bartels 2017). The fact that we found lower values of Σ in the fovea of V1 for VFM supports this view (Gilbert and Li 2013).

Relation of the BOLD Autocovariance Decay Constant to Behavioral Condition

The temporal decay constants of the autocovariance (τ), derived empirically from the RS and VFM data, determined the rate at which the fluctuations diffused through the noise-diffusion network model. Higher values of τ imply longer temporal memory (i.e., the system's past dynamics have a stronger influence on its future dynamics). Importantly, the determination of consistent decay constants for RS and VFM demonstrated that propagation was present in both cases, at similar temporal scales. However, estimates of τ obtained from VFM data were slightly greater (albeit not significantly higher) than those derived from RS data (Fig. 2*B*), suggesting longer temporal memory during VFM. This

is in contrast to previous studies showing that temporal memory decreases during task compared to RS (He et al. 2010; He 2011). By estimating task-induced decreases in the power-law exponent of BOLD fluctuations across widespread brain regions, these studies suggest that the temporal memory is longest during RS. They relate the larger power-law exponent found in RS to higher time-lagged autocovariances and interpret this as longer temporal memory. One possible reason for this differing results is that He and colleagues examined widespread whole-brain interactions, whereas here we examined BOLD signal dynamics at a more local scale (the cortical surface of individual visual field maps) and with higher resolution (7T). Furthermore, our results are specific to early visual cortex and therefore may not generalize to the whole brain. Another possible explanation is that these studies were based on eyes-open RS (fixation on a white cross-hair in the center of black screen) whereas we used eyes-closed RS. These different measurement scales and task protocols may well explain the observed differences.

In our study, the slight increase in temporal memory found in VFM may likely reflect stimulus induced interactions. By giving rise to slow frequency fluctuations in the BOLD signal that are spatially correlated with the stimulus position, these interactions may lead to higher temporal redundancy and therefore longer memory depth (higher τ). On the other hand, the absence of stimulus induced interactions during RS may lead to a decrease in spatiotemporally correlated slow fluctuations, locked to the stimuli during VFM, leaving intrinsic fluctuations and fast transitions to dominate the temporal autocovariance structure (thus reducing τ during RS). Finally, the aforementioned studies (He et al. 2010; He 2011), computed the power-law exponent of the fMRI time series by using the low frequency range (<0.1 Hz) of the power spectrum, whereas we computed τ from minimally preprocessed BOLD time series to which only detrending and demeaning was applied. By avoiding such low-pass filtering, we allowed faster fluctuations to influence our estimates of τ. All these lines of evidence suggest that, in early visual cortex, the temporal scale of BOLD activity propagation differs between RS and VFM. Compared to the slow and spatially widespread (long) propagation patterns evoked by the VFM stimulus, intrinsic fluctuations during RS tend to unfold locally in space and time. These shorter and more localized propagation events may dominate the spatiotemporal covariance structure and explain the increased EC within-area interactions observed during RS.

Limitations and Interpretability of the Model

An important limitation in the present study was the fact that we only acquired data from a limited field of view, which forced us to consider a subset of all existing connections. This might have neglected the contribution of indirect influences to estimated changes in the EC, as dependencies may arise from indirect interactions in the underlying anatomy. In addition to direct corticocortical connections (e.g., from V2 to V1), feedback can cascade over a succession of cortical areas and subcortical pathways (Sherman and Guillery 2011; Saalmann et al. 2012; Gilbert and Li 2013). Similarly, the increased Σ values identified during RS in the foveal representation of V1 may reflect changes in input from other brain regions as well.

Other possible limitations derived from the fact that our approach was different from the original implementation of the noise-diffusion network model (Gilson et al. 2016, 2018) in two aspects: 1) Diffusion tensor imaging (DTI) cannot estimate structural connectivity at the spatial scales involved here. Therefore, our implementation was topologically agnostic compared to these previous studies: no structural connectivity matrix (i.e., DTI-derived) was used to constrain the EC; 2) we apply the approach to the scale of individual visual field maps whereas it was originally devised for whole-brain analyses (ROI ~ 500–1000 voxels instead of ~50 here) (Gilson et al. 2016, 2018). However, we think the approach is still valid since there are known strong anatomical connections between V1, V2, and V3. Also, regional variation in the hemodynamic response is less pronounced at this scale (Lin et al. 2017), which further justifies the implementation of the model.

Another limitation is that we only allowed positive weights to be adjusted in the EC, which lead us to interpret the intrinsic variability of the model (Σ) to the aggregate changes in cortical excitability across both inhibitory and excitatory neuronal populations. We justify this decision based on the metabolic underpinnings of the BOLD signal: inhibitory functions, which are supported more by oxidative mechanisms than by excitatory signaling, may contribute less than excitatory functions to the measured BOLD activity (Buzsáki et al. 2007). Therefore, excitatory glutamatergic input to principal neurons might influence EC more than modulatory functions, which are exerted by a mostly inhibitory interneuronal network (Buzsáki et al. 2007; Sherman and Guillery 2011). Furthermore, allowing negative correlations between one voxel and another allows connections between a voxel where the stimulus is in the center of the pRF and a voxel where the stimulus is in the suppressive surround. Suppressive surrounds are large, so this is likely to lead to widespread spurious EC. Based on these reasons, we believe that positive weights in the EC are enough to capture the underlying neuronal interactions that shape BOLD responses.

We note that our aim was not to infer the detailed causal mechanism that gives rise to the propagation of BOLD activity. Rather, our aim has been to assess the utility of a specific EC framework (a topologically agnostic noise-diffusion network) to quantify BOLD activity propagation at the level of individual cortical areas. In this regard, we note that local variation in neurovascular coupling profiles may hinder our analysis (Schölvinck et al. 2010; Aquino et al. 2012; Pang et al. 2017), as they would affect the EC values (but less likely their modulations across conditions). Nevertheless, we do not model the hemodynamic response function (HRF) for a number of reasons. First, we assume the HRF to be relatively constant across V1, V2, and V3, even though the underlying vascular network may introduce certain non-uniformity (Harrison et al. 2002; Handwerker et al. 2004; Tong et al. 2016; Lin et al. 2017). Second, our model reproduces the empirical spatiotemporal covariance analytically, and therefore does not rely on generative models of neuronal activity and neurovascular coupling to simulate the BOLD time series (this is why only actual BOLD data are shown in Fig. 1). While such an approach would be valuable to address questions of mechanistic causality, we think that the current temporal and spatial resolution of fMRI leaves such questions out of reach. In future studies, extending this or similar approaches with high spatial resolution fMRI might help disclose brain interactions specific to separate cortical layers, allowing to dissociate lateral, feedforward, and feedback interactions at a more fine-grained scale than previously possible in human sensory cortex (Lawrence et al. 2017; Fracasso et al. 2018; Mitra et al. 2018; Petridou and Siero 2019).

The time- and task-dependent nature of BOLD activity propagation patterns poses the question of how closely directed

interactions map onto structural connections (Adachi et al. 2012). An emerging view suggests that structural connection patterns are indeed major constraints for the dynamics of brain activity (Deco et al. 2017), which are partly captured by functional and EC. However, whether BOLD propagation is generated only through temporally ordered processes of neuronal origin unfolding through underlying neuroanatomical networks or also through additional changes in physiological, metabolic, or vascular variables remains an issue of debate (Matsui et al. 2016). Indeed, the precise neuronal mechanisms that determine the spatial and temporal distribution of BOLD signal co-fluctuations and propagation are not yet fully understood. If BOLD fluctuations reflect the consequences of spiking activity, aggregate subthreshold fluctuations (Logothetis et al. 2001), or metabolic relationships among neurons, astrocytes and the supporting capillary network (i.e., neuro-vascular coupling) (OHerron et al. 2016; Pang et al. 2017), is an area of ongoing research. On the one hand, BOLD activity propagation patterns within areas during VFM, together with transient, retinotopically selective, coactivation between different visual areas, appear to reflect retinotopically organized switching of the spiking input activity between voxels sharing similar visual field position selectivity and tuning characteristics (Kenet et al. 2003; Blumenfeld et al. 2006; Lewis et al. 2016; Vinck and Bosman 2016). On the other hand, during RS, BOLD propagation patterns may reflect the footprint of slow subthreshold fluctuations in local field potentials, which can be retinotopically organized and are known to be good predictors of the BOLD signal spatiotemporal covariance structure (Logothetis and Wandell 2004; Carandini et al. 2015). Indeed, a recent study by Matsui and colleagues (2016) using neuronal calcium signals and simultaneous hemodynamic recordings brings together these lines of evidence by demonstrating that both global fluctuations, in the form of waves propagating across cortex, and transient local coactivations in calcium signals are necessary for setting the spatiotemporal covariance structure of hemodynamic signals (Matsui et al. 2016). Another line of evidence points to neuronal mechanisms of interareal coupling and modulation reflected in the estimated changes in EC. A recent study analyzed simultaneous recordings from V1 and V4 in monkeys and showed that feedforward interactions from V1 to V4 were based on frequencies around the gamma band (van Kerkoerle et al. 2014; Michalareas et al. 2016), whereas feedback interactions from V4 to V1 were supported by alpha activity (Buffalo et al. 2011; Xing et al. 2012). These studies highlight the important fact that different temporal processes may be used as channels over which "information" flows between visual cortical areas. Therefore, care should be taken when interpreting the nature of the estimated interactions in EC.

Furthermore, non-neuronal mechanisms such as the wave-like propagation of hemodynamic activity originating in pial arterioles has been described (Rayshubskiy et al. 2014) and related to oscillations in systemic blood pressure (the so called "Mayer waves") (Julien 2006). Similarly, large veins draining to the dural sinuses near the occipital pole, which are known to modulate the phase of nearby hemodynamic fluctuations with little effect on signal amplitude (Menon et al. 1995; Winawer et al. 2010), may also play a role in shaping, for instance, the parafovea-to-fovea interactions observed during RS. Moreover, acting as a temporal low-pass filter, neurovascular coupling mechanisms involving the activity of astrocytes (Pang et al. 2017) and the diffusion of vasodilatory signaling molecules (i.e., nitric oxide) may play an important role in setting the pace of BOLD activity propagation patterns. Together, all these lines of evidence point to the importance of considering the multiple physiological factors implicated in shaping the BOLD signal when interpreting patterns of BOLD activity propagation.

The different propagation patterns of BOLD activity during RS and VFM, as assessed with the present EC analysis, demonstrate distinct cortical dynamics during visual stimulation and in its absence (Kenet et al. 2003; Lewis et al. 2016). Nevertheless, in a previous analysis of the present dataset, we found that BOLD activity across cortical locations of V1, V2, and V3 sharing similar visual field selectivity (functionally homotopic) can co-fluctuate during RS, enabling the estimation of connective field models from RS data (see Fig. 3 in Gravel et al. 2014) that resemble those obtained from VFM data. The fact that retinotopically congruent co-fluctuations in BOLD activity across visual cortical areas can also occur during RS (Heinzle et al. 2011; Gravel et al. 2014; Butt et al. 2015) suggests that non-retinal and "top–down" influences, such as feedback modulation of V1 responses, may also play a role generating structured patterns of BOLD propagation during rest (Muckli and Petro 2013). During RS, a variety of behavioral processes, such as memory consolidation and learning, may recruit V1 into a processing stream—even without external visual stimulation (Kosslyn et al. 1995; Slotnick et al. 2005; Petro et al. 2014). Together, these studies suggest that, during RS, periods of highly organized neuronal activity in the visual cortex give rise to transitory periods of retinotopically organized BOLD activity propagation. Co-fluctuations within and between early cortical visual field maps may follow, likely reflecting different states of cortical processing (Gilbert and Sigman 2007; Gilbert and Li 2013; Schölvinck et al. 2015).

Finally, the current study assesses BOLD propagation in eight healthy participants. Although our results are consistent across participants, further studies involving more participants or datasets such as the 7T HCP retinotopy dataset are warranted. Moreover, the EC models were estimated based on grouped RS and VFM scans. As such, they estimate average BOLD propagation patterns and do not capture specific intervals of variation in these. To establish the neuronal mechanisms underlying the observed changes in EC, further research using high spatial resolution fMRI and different tasks inviting behaviorally relevant responses are advised.

Concluding Remarks

We have shown that the propagation of BOLD activity through early visual cortex reveals different directed interaction regimes across the topography and hierarchy of visual cortical areas V1, V2, and V3 during both RS and VFM. We relate these differences in the estimated EC to a task-dependent reconfiguration of feed-forward and feedback interactions throughout the visual system and changes in Σ to a task-dependent neuronal modulation of local cortical excitability. Our results add to a growing body of evidence suggesting that recurrent connectivity and cortico-cortical feedback plays a central role in visual processing. They are consistent with the hypothesis that directed influences (i.e., feedback to V1), as well as intrinsic connectivity (i.e., cortical excitability), interact differently during visual stimulation and rest as a consequence of the visual system using an active inference strategy to process incoming stimuli. We conclude by answering our original question of how the propagation of BOLD activity can also reveal relevant aspects of brain activity at a

more local scale. By acknowledging the existence of propagated disturbances in BOLD activity, our approach provides a simple method to infer the local excitability of visual cortical areas and the directed influences unfolding among them during distinct behavioral states.

Funding

(Chilean) National Commission for Scientific and Technological Research (BECAS CHILE) and the Graduate School for Medical Sciences (GSMS) of the University Medical Center Groningen (UMCG) (to N.G.); The Netherlands Organization for Scientific Research (NWO Brain and Cognition grant 433-09-233 to B.M.H., R.J.R. and F.W.C.); Portuguese Foundation for Science and Technology (Investigator grant #IF/01405/2014 to B.M.H.); the Netherlands Organization for Scientific Research (VIDI grant 452-17-012 to B.M.H.); Spanish Research Project (PSI2016-75688-P to G.D.) (Agencia Estatal de Investigación/Fondo Europeo de Desarrollo Regional, European Union); European Union's Horizon 2020 Research and Innovation Programme under Grant Agreements 720270 (Human Brain Project [HBP] SGA1) and 785907 (HBP SGA2); the Catalan Agencia de Gestión de Ayudas Universitarias Programme 2017 SGR 1545.

Conflict of Interest

None declared.

References

Adachi Y, Osada T, Sporns O, Watanabe T, Matsui T, Miyamoto K, Miyashita Y. 2012. Functional connectivity between anatomically unconnected areas is shaped by collective network-level effects in the macaque cortex. *Cereb Cortex*. 22(7):1586–1592.

Aguirre GK, Zarahn E, D'Esposito M. 1998. The variability of human, BOLD hemodynamic responses. *Neuroimage*. 8(4):360–369.

Al-Aidroos N, Said CP, Turk-Browne NB. 2012. Top-down attention switches coupling between low-level and high-level areas of human visual cortex. *Proc Natl Acad Sci USA*. 109(36): 14675–14680.

Angelucci A, Bressloff PC. 2006. Contribution of feedforward, lateral and feedback connections to the classical receptive field center and extra-classical receptive field surround of primate V1 neurons. *Prog Brain Res*. 154:93–120.

Aquino KM, Schira MM, Robinson PA, Drysdale PM, Breakspear M. 2012. Hemodynamic traveling waves in human visual cortex. *PLoS Comput Biol*. 8(3):e1002435.

Biswal B, Zerrin Yetkin F, Haughton VM, Hyde JS. 1995. Functional connectivity in the motor cortex of resting human brain using echo-planar mri. *Magn Reson Med*. 34(4):537–541.

Blumenfeld B, Bibitchkov D, Tsodyks M. 2006. Neural network model of the primary visual cortex: from functional architecture to lateral connectivity and back. *J Comput Neurosci*. 20(2):219–241.

Braddick OJ, O'Brien JMD, Wattam-Bell J, Atkinson J, Hartley T, Turner R. 2001. Brain areas sensitive to coherent visual motion. *Perception*. 30(1):61–72.

Brainard DH. 1997. The psychophysics toolbox. *Spat Vis*. 10(4):433–436.

Buffalo EA, Fries P, Landman R, Buschman TJ, Desimone R. 2011. Laminar differences in gamma and alpha coherence in the ventral stream. *Proc Natl Acad Sci USA*. 108(27):11262–11267.

Butt OH, Benson NC, Datta R, Aguirre GK. 2015. Hierarchical and homotopic correlations of spontaneous neural activity within the visual cortex of the sighted and blind. *Front Hum Neurosci*. 9:25.

Buzsáki G, György B, Kai K, Marcus R. 2007. Inhibition and brain work. *Neuron*. 56(5):771–783.

Carandini M, Shimaoka D, Rossi LF, Sato TK, Benucci A, Knöpfel T. 2015. Imaging the awake visual cortex with a genetically encoded voltage indicator. *J Neurosci*. 35(1):53–63.

Cardin V, Friston KJ, Zeki S. 2011. Top-down modulations in the visual form pathway revealed with dynamic causal modeling. *Cereb Cortex*. 21(3):550–562.

Dayan P, Hinton GE, Neal RM, Zemel RS. 1995. The Helmholtz machine. *Neural Comput*. 7(5):889–904.

Deco G, Kringelbach ML, Jirsa VK, Ritter P. 2017. The dynamics of resting fluctuations in the brain: metastability and its dynamical cortical core. *Sci Rep*. 7(1):3095.

Dumoulin SO, Wandell BA. 2008. Population receptive field estimates in human visual cortex. *Neuroimage*. 39(2):647–660.

Ermentrout GB, Cowan JD. 1979. Temporal oscillations in neuronal nets. *J Math Biol*. 7(3):265–280.

Fracasso A, Luijten PR, Dumoulin SO, Petridou N. 2018. Laminar imaging of positive and negative BOLD in human visual cortex at 7T. *Neuroimage*. 164:100–111.

Friston KJ. 2005. A theory of cortical responses. *Philos Trans R Soc Lond B Biol Sci*. 360(1456):815–836.

Friston KJ, Harrison L, Penny W. 2003. Dynamic causal modelling. *Neuroimage*. 19:1273–1302.

Friston KJ, Kilner J, Harrison L. 2006. A free energy principle for the brain. *J Physiol Paris*. 100(1–3):70–87.

Genç E, Schölvinck ML, Bergmann J, Singer W, Kohler A. 2016. Functional connectivity patterns of visual cortex reflect its anatomical organization. *Cereb Cortex*. 36(9):3719–3731.

Gilbert CD, Li W. 2013. Top-down influences on visual processing. *Nat Rev Neurosci*. 14(5):350–363.

Gilbert CD, Sigman M. 2007. Brain states: top-down influences in sensory processing. *Neuron*. 54(5):677–696.

Gilbert CD, Wiesel TN. 1992. Receptive field dynamics in adult primary visual cortex. *Nature*. 356(6365):150–152.

Gilson M, Deco G, Friston KJ, Hagmann P, Mantini D, Betti V, Romani GL, Corbetta M. 2018. Effective connectivity inferred from fMRI transition dynamics during movie viewing points to a balanced reconfiguration of cortical interactions. *Neuroimage*. 180:534–546.

Gilson M, Moreno-Bote R, Ponce-Alvarez A, Ritter P, Deco G. 2016. Estimation of directed effective connectivity from fMRI functional connectivity hints at asymmetries of cortical connectome. *PLoS Comput Biol*. 12(3):e1004762.

Goebel R, Roebroeck A, Kim DS, Formisano E. 2003. Investigating directed cortical interactions in time-resolved fMRI data using vector autoregressive modeling and granger causality mapping. *Magn Reson Imaging*. 21(10):1251–1261.

Gravel N, Harvey B, Nordhjem B, Haak KV, Dumoulin SO, Renken R, Curčić-Blake B, Cornelissen FW. 2014. Cortical connective field estimates from resting state fMRI activity. *Front Neurosci*. 8:339.

Haak KV, Marquand AF, Beckmann CF. 2017. Connectopic mapping with resting-state fMRI. *Neuroimage*. 170: 83–94.

Haegens S, Nácher V, Luna R, Romo R, Jensen O. 2011. α-Oscillations in the monkey sensorimotor network influence discrimination performance by rhythmical inhibition of neuronal spiking. *Proc Natl Acad Sci USA*. 108(48):19377–19382.

Handwerker DA, Ollinger JM, D'Esposito M. 2004. Variation of BOLD hemodynamic responses across subjects and brain regions and their effects on statistical analyses. *Neuroimage*. 21(4):1639–1651.

Harrison RV, Harel N, Panesar J, Mount RJ. 2002. Blood capillary distribution correlates with hemodynamic-based functional imaging in cerebral cortex. *Cereb Cortex*. 12(3):225–233.

Harrison L, Penny WD, Friston KJ. 2003. Multivariate autoregressive modeling of fMRI time series. *Neuroimage*. 19(4):1477–1491.

Harrison LM, Stephan KE, Rees G, Friston KJ. 2007. Extra-classical receptive field effects measured in striate cortex with fMRI. *Neuroimage*. 34(3):1199–1208.

Harvey BM, Dumoulin SO. 2011. The relationship between cortical magnification factor and popu-lation receptive field size in human visual cortex: constancies in cortical architecture. *J Neurosci*. 31(38):13604–13612.

Harvey BM, Vansteensel MJ, Ferrier CH, Petridou N, Zuiderbaan W, Aarnoutse EJ, Bleichner MG, Dijkerman HC, van Zandvoort MJE, Leijten FSS *et al*. 2013. Frequency specific spatial interactions in human electrocorticography: V1 alpha oscillations reflect surround suppression. *Neuroimage*. 65: 424–432.

Haynes JD, Driver J, Rees G. 2005. Visibility reflects dynamic changes of effective connectivity between V1 and fusiform cortex. *Neuron*. 46(5):811–821.

He BJ. 2011. Scale-free properties of the functional magnetic resonance imaging signal during rest and task. *J Neurosci*. 31(39):13786–13795.

He BJ, Zempel JM, Snyder AZ, Raichle ME. 2010. The temporal structures and functional significance of scale-free brain activity. *Neuron*. 66(3):353–369.

Heinzle J, Kahnt T, Haynes JD. 2011. Topographically specific functional connectivity between visual field maps in the human brain. *Neuroimage*. 56(3):1426–1436.

Heitmann S, Ermentrout GB. 2015. Synchrony, waves and ripple in spatially coupled Kuramoto oscillators with Mexican hat connectivity. *Biol Cybern*. 109(3):333–347.

Hindriks R, Mantini R, Gravel N, Deco G. 2019. Latency analysis of resting-state BOLD-fMRI reveals traveling waves in visual cortex linking task-positive and task-negative networks. *Neuroimage*. 200:259–274.

Hindriks R, van Putten MJAM, Deco G. 2014. Intra-cortical propagation of EEG alpha oscillations. *Neuroimage*. 103:444–453.

Jadhav SP, Kemere C, German PW, Frank LM. 2012. Awake hippocampal sharp-wave ripples support spatial memory. *Science*. 336(6087):1454–1458.

Julien C. 2006. The enigma of Mayer waves: facts and models. *Cardiovasc Res*. 70(1):12–21.

Kaplan R, Adhikari MH, Hindriks R, Mantini D, Murayama Y, Logothetis NK, Deco G. 2016. Hippocampal sharp-wave ripples influence selective activation of the default mode network. *Curr Biol*. 26(5):686–691.

Kastner S, Pinsk MA, De Weerd P, Desimone R, Ungerleider LG. 1999. Increased activity in human visual cortex during directed attention in the absence of visual stimulation. *Neuron*. 22:751–761.

Kenet T, Bibitchkov D, Tsodyks M, Grinvald A, Arieli A. 2003. Spontaneously emerging cortical representations of visual attributes. *Nature*. 425(6961):954–956.

Kosslyn SM, Thompson WL, Kim IJ, Alpert NM. 1995. Topographical representations of mental images in primary visual cortex. *Nature*. 378(6556):496–498.

Lamme VA, Supèr H, Spekreijse H. 1998. Feedforward, horizontal, and feedback processing in the visual cortex. *Curr Opin Neurobiol*. 8(4):529–535.

Lauritzen TZ, D'Esposito M, Heeger DJ, Silver MA. 2009. Top-down flow of visual spatial attention signals from parietal to occipital cortex. *J Vis*. 9(13):18–18.

Lawrence SJ, Formisano E, Muckli L, de Lange FP. 2017. Laminar fMRI: applications for cognitive neuroscience. *Neuroimage*. 197:785–791.

Le Bihan D, Mangin JF, Poupon C, Clark CA, Pappata S, Molko N, Chabriat H. 2001. Diffusion tensor imaging: concepts and applications. *J Magn Reson Imaging*. 13(4):534–546.

Lee TS, Mumford D. 2003. Hierarchical bayesian inference in the visual cortex. *J Opt Soc Am A Opt Image Sci Vis*. 20(7):1434–1448.

Lewis CM, Bosman CA, Womelsdorf T, Fries P. 2016. Stimulus-induced visual cortical networks are recapitulated by spontaneous local and interareal synchronization. *Proc Natl Acad Sci USA*. 113(5):E606–E615.

Lin FH, Polimeni JR, Lin JFL, Tsai KWK, Chu YH, Wu PY, Li YT, Hsu YC, Tsai SY, Kuo WJ. 2017. Relative latency and temporal variability of hemodynamic responses at the human primary visual cortex. *Neuroimage*. 164:194–201.

Logothetis NK, Eschenko O, Murayama Y, Augath M, Steudel T, Evrard HC, Besserve M, Oeltermann A. 2012. Hippocampal-cortical interaction during periods of subcortical silence. *Nature*. 491(7425):547–553.

Logothetis NK, Pauls J, Augath M, Trinath T, Oeltermann A. 2001. Neurophysiological investigation of the basis of the fMRI signal. *Nature*. 412(6843):150–157.

Logothetis NK, Wandell BA. 2004. Interpreting the BOLD signal. *Annu Rev Physiol*. 66:735–769.

Massimini M, Huber R, Ferrarelli F, Hill S, Tononi G. 2004. The sleep slow oscillation as a traveling wave. *J Neurosci*. 24(31):6862–6870.

Matsui T, Murakami T, Ohki K. 2016. Transient neuronal coactivations embedded in globally propagating waves underlie resting-state functional connectivity. *Proc Natl Acad Sci USA*. 113(23):6556–6561.

Meehan TP, Bressler SL, Tang W, Astafiev SV, Sylvester CM, Shulman GL, Corbetta M. 2017. Top-down cortical interactions in visuospatial attention. *Brain Struct Funct*. 222(7):3127–3145.

Menon RS, Ogawa S, Ugurbil K. 1995. High-temporal-resolution studies of the human primary visual cortex at 4 T: teasing out the oxygenation contribution in FMRI. *Int J Imaging Systems Technol*. 6(2–3):209–215.

Michalareas G, Vezoli J, van Pelt S, Schoffelen JM, Kennedy H, Fries P. 2016. Alpha-Beta and Gamma rhythms subserve feedback and feedforward influences among human visual cortical areas. *Neuron*. 89(2):384–397.

Mitra A, Kraft A, Wright P, Acland B, Snyder AZ, Rosenthal Z, Czerniewski L, Bauer A, Snyder L, Culver J *et al*. 2018. Spontaneous infra-slow brain activity has unique spatiotemporal dynamics and laminar structure. *Neuron*. 98(2): 297–305.e6.

Mitra A, Snyder AZ, Hacker CD, Pahwa M, Tagliazucchi E, Laufs H, Leuthardt EC, Raichle ME. 2016. Human cortical-hippocampal dialogue in wake and slow-wave sleep. *Proc Natl Acad Sci USA*. 113(44):E6868–E6876.

Mitra A, Snyder AZ, Tagliazucchi E, Laufs H, Raichle ME. 2015. Propagated infra-slow intrinsic brain activity reorganizes across wake and slow wave sleep. *Elife*. 4:e10781.

Muckli L, Petro LS. 2013. Network interactions: non-geniculate input to V1. *Curr Opin Neurobiol*. 23(2):195–201.

Mumford D. 1994. Pattern theory: A unifying perspective. In: Joseph A, Mignot F, Murat F, Prum B, Rentschler R, editors. *First European Congress of Mathematics. Progress in Mathematics*, Vol 3. Birkhäuser, Basel doi: https://doi.org/10.1007/978-3-0348-9110-3_6.

Nestares O, Heeger DJ. 2000. Robust multiresolution alignment of MRI brain volumes. *Magn Reson Med*. 43(5):705–715.

Nichols TE, Holmes AP. 2001. Nonparametric permutation tests for functional neuroimaging experiments: a primer with examples. *Hum Brain Mapp*. 15(1):1–25.

OHerron P, Philip O, Chhatbar PY, Manuel L, Zhiming S, Schramm AE, Zhongyang L, Prakash K. 2016. Neural correlates of single-vessel haemodynamic responses in vivo. *Nature*. 534: 378–382.

Pang JC, Robinson PA, Aquino KM, Vasan N. 2017. Effects of astrocytic dynamics on spatiotemporal hemodynamics: modeling and enhanced data analysis. *Neuroimage*. 147:994–1005.

Pelli DG. 1997. The VideoToolbox software for visual psychophysics: transforming numbers into movies. *Spat Vis*. 10(4):437–442.

Penny WD, Stephan KE, Mechelli A, Friston KJ. 2004. Modelling functional integration: a comparison of structural equation and dynamic causal models. *Neuroimage*. 23:264–274.

Peter A, Uran C, Klon-Lipok J, Roese R, van Stijn S, Barnes W, Dowdall JR, Singer W, Fries P, Vinck M. 2019. Surface color and predictability determine contextual modulation of V1 firing and gamma oscillations. *Elife*. 8:e42101.

Petridou N, Siero JC. 2019. Laminar fMRI: what can the time domain tell us? *Neuroimage*. 197:761–771.

Petro LS, Muckli L. 2016. The brain's predictive prowess revealed in primary visual cortex. *Proc Natl Acad Sci USA*. 113(5):1124–1125.

Petro LS, Vizioli L, Muckli L. 2014. Contributions of cortical feedback to sensory processing in primary visual cortex. *Front Psychol*. 5:1223.

Raichle ME. 2000. A brief history of human functional brain mapping. In: Toga AW, Mazziotta CJ, editors. *Brain Mapping: The Systems*. San Diego Academic Press, pp. 33–75.

Rao RP, Ballard DH. 1999. Predictive coding in the visual cortex: a functional interpretation of some extra-classical receptive-field effects. *Nat Neurosci*. 2(1):79–87.

Rayshubskiy A, Wojtasiewicz TJ, Mikell CB, Bouchard MB, Timerman D, Youngerman BE, McGovern RA, Otten ML, Canoll P, McKhann GM *et al*. 2014. Direct, intraoperative observation of ˜0.1hz hemodynamic oscillations in awake human cortex: implications for fMRI. *Neuroimage*. 87:323–331.

Revina Y, Petro LS, Muckli L. 2017. Cortical feedback signals generalise across different spatial frequencies of feedforward inputs. *Neuroimage*. 180:280–290.

Saalmann YB, Ma P, Wang L, Li X, Kastner S. 2012. The pulvinar regulates information transmission between cortical areas based on attention demands. *Science*. 337:753–756.

Schellekens W, van Wezel RJA, Petridou N, Ramsey NF, Raemaekers M. 2016. Predictive coding for motion stimuli in human early visual cortex. *Brain Struct Funct*. 221(2):879–890.

Schindler A, Bartels A. 2017. Connectivity reveals sources of predictive coding signals in early visual cortex during processing of visual optic flow. *Cereb Cortex*. 27(5):2885–2893.

Schira MM, Tyler CW, Spehar B, Breakspear M. 2010. Modeling magnification and anisotropy in the primate foveal confluence. *PLoS Comput Biol*. 6(1):e1000651.

Schölvinck ML, Maier A, Ye FQ, Duyn JH, Leopold DA. 2010. Neural basis of global resting-state fMRI activity. *Proc Natl Acad Sci USA*. 107(22):10238–10243.

Schölvinck ML, Saleem AB, Benucci A, Harris KD, Carandini M. 2015. Cortical state determines global variability and correlations in visual cortex. *J Neurosci*. 35(1):170–178.

Schwabe L, Ichida JM, Shushruth S, Mangapathy P, Angelucci A. 2010. Contrast-dependence of surround suppression in macaque v1: experimental testing of a recurrent network model. *Neuroimage*. 52(3):777–792.

Schwabe L, Obermayer K, Angelucci A, Bressloff PC. 2006. The role of feedback in shaping the extra-classical receptive field of cortical neurons: a recurrent network model. *J Neurosci*. 26(36):9117–9129.

Seth AK, Barrett AB, Barnett L. 2015. Granger causality analysis in neuroscience and neuroimaging. *J Neurosci*. 35(8): 3293–3297.

Sherman SM, Guillery RW. 2011. Distinct functions for direct and transthalamic corticocortical connections. *J Neurophysiol*. 106(3):1068–1077.

Slotnick SD, Thompson WL, Kosslyn SM. 2005. Visual mental imagery induces retinotopically organized activation of early visual areas. *Cereb Cortex*. 15(10):1570–1583.

Smith SM, Miller KL, Salimi-Khorshidi G, Webster M, Beckmann CF, Nichols TE, Ramsey JD, Woolrich MW. 2011. Network modelling methods for FMRI. *Neuroimage*. 54(2): 875–891.

Stephan KE. 2005. Investigating the functional role of callosal connections with dynamic causal models. *Ann N Y Acad Sci*. 1064(1):16–36.

Steriade M. 2000. Corticothalamic resonance states of vigilance and mentation. *Neuroscience*. 101(2):243–276.

Teo PC, Sapiro G, Wandell BA. 1997. Creating connected representations of cortical gray matter for functional MRI visualization. *IEEE Trans Med Imaging*. 16(6): 852–863.

Tong Y, Hocke LM, Lindsey KP, Erdoğan SB, Vitaliano G, Caine CE, Frederick BD. 2016. Systemic low-frequency oscillations in BOLD signal vary with tissue type. *Front Neurosci*. 10:313.

Tong Y, Yunjie T, Frederick BD. 2014. Studying the spatial distribution of physiological effects on BOLD signals using ultrafast fMRI. *Front Hum Neurosci*. 8:196.

van Kerkoerle T, Self MW, Dagnino B, Gariel-Mathis MA, Poort J, van der Togt C, Roelfsema PR. 2014. Alpha and gamma oscillations characterize feedback and feedforward processing in monkey visual cortex. *Proc Natl Acad Sci USA*. 111(40):14332–14341.

Vincent JL, Patel GH, Fox MD, Snyder AZ, Baker JT, Van Essen DC, Zempel JM, Snyder LH, Corbetta M, Raichle ME. 2007. Intrinsic functional architecture in the anaesthetized monkey brain. *Nature*. 447(7140):83–86.

Vinck M, Bosman CA. 2016. More gamma more predictions: gamma-synchronization as a key mechanism for efficient integration of classical receptive field inputs with surround predictions. *Front Syst Neurosci*. 10:35.

Vinje WE, Gallant JL. 2000. Sparse coding and Decorrelation in primary visual cortex during natural vision. *Science*. 287(5456):1273–1276.

Von Helmholtz H. 1867. *Handbuch der physiologischen Optik*. Leipzig: Leopold Voss.

Wandell BA, Chial S, Backus BT. 2000. Visualization and measurement of the cortical surface. *J Cogn Neurosci*. 12(5):739–752.

Williamson SJ, Kaufman L, Lu ZL, Wang JZ, Karron D. 1997. Study of human occipital alpha rhythm: the alphon hypothesis and alpha suppression. *Int J Psychophysiol*. 26(1–3):63–76.

Winawer J, Horiguchi H, Sayres RA, Wandell BA. 2010. Mapping hV4 and ventral occipital cortex : the venous eclipse. *J Vis*. 10(5):1–22.

Xing D, Yeh CI, Burns S, Shapley RM. 2012. Laminar analysis of visually evoked activity in the primary visual cortex. *Proc Natl Acad Sci USA*. 109(34): 13871–13876.

Yeo BTT, Krienen FM, Sepulcre J, Sabuncu MR, Lashkari D, Hollinshead M, Roffman JL, Smoller JW, Zöllei L, Polimeni JR *et al*. 2011. The organization of the human cerebral cortex estimated by intrinsic functional connectivity. *J Neurophysiol*. 106(3):1125–1165.